Monthly Notices
of the
ROYAL ASTRONOMICAL SOCIETY

MNRAS **487,** 5824–5839 (2019)
Advance Access publication 2019 June 10

doi:10.1093/mnras/stz1588

GRB 161219B/SN 2016jca: a powerful stellar collapse

C. Ashall,[1,2]★ P. A. Mazzali,[2,3] E. Pian,[4] S. E. Woosley,[5] E. Palazzi,[4] S. J. Prentice,[2,6] S. Kobayashi,[2] S. Holmbo,[7] A. Levan,[8] D. Perley,[2] M. D. Stritzinger,[7] F. Bufano,[9] A. V. Filippenko,[10,11] A. Melandri,[12] S. Oates,[8] A. Rossi,[4] J. Selsing,[13] W. Zheng,[10] A. J. Castro-Tirado,[14] G. Chincarini,[12] P. D'Avanzo,[12] M. De Pasquale,[15] S. Emery,[16] A. S. Fruchter,[17] K. Hurley,[18] P. Moller,[19] K. Nomoto,[20] M. Tanaka[21] and A. F. Valeev[22]

Affiliations are listed at the end of the paper

Accepted 2019 June 4. Received 2019 June 4; in original form 2019 April 1

ABSTRACT

We report observations and analysis of the nearby gamma-ray burst GRB 161219B (redshift $z = 0.1475$) and the associated Type Ic supernova (SN) 2016jca. GRB 161219B had an isotropic gamma-ray energy of $\sim 1.6 \times 10^{50}$ erg. Its afterglow is likely refreshed at an epoch preceding the first photometric points (0.6 d), which slows down the decay rates. Combined analysis of the SN light curve and multiwavelength observations of the afterglow suggest that the GRB jet was broad during the afterglow phase (full opening angle $\sim 42^\circ \pm 3^\circ$). Our spectral series shows broad absorption lines typical of GRB supernovae (SNe), which testify to the presence of material with velocities up to $\sim$0.25c. The spectrum at 3.73 d allows for the very early identification of an SN associated with a GRB. Reproducing it requires a large photospheric velocity ($35\,000 \pm 7000$ km s^{-1}). The kinetic energy of the SN is estimated through models to be $E_{\rm kin} \approx 4 \times 10^{52}$ erg in spherical symmetry. The ejected mass in the explosion was $M_{\rm ej} \approx 6.5 \pm 1.5$ M$_\odot$, much less than that of other GRB-SNe, demonstrating diversity among these events. The total amount of ^{56}Ni in the explosion was 0.27 ± 0.05 M$_\odot$. The observed spectra require the presence of freshly synthesized ^{56}Ni at the highest velocities, at least three times more than a standard GRB-SN. We also find evidence for a decreasing ^{56}Ni abundance as a function of decreasing velocity. This suggests that SN 2016jca was a highly aspherical explosion viewed close to on-axis, powered by a compact remnant. Applying a typical correction for asymmetry, the energy of SN 2016jca was $\sim (1\text{–}3) \times 10^{52}$ erg, confirming that most of the energy produced by GRB-SNe goes into the kinetic energy of the SN ejecta.

Key words: supernovae: general – supernovae: individual: . . ..

1 INTRODUCTION

When massive stars, with helium cores smaller than 65 M$_\odot$, exhaust their nuclear fuel their cores collapse to a compact object (a neutron star or a black hole; Woosley 2017). The collapse triggers a supernova (SN) explosion, in which the outer layers of the star are expelled and a luminous display is created. If the SN is of Type I, the main power source for its luminosity is usually the radioactive decay of ^{56}Ni, which is synthesized in the stellar layers above the compact remnant, or along the jet axis, and ejected in the SN (Barnes et al. 2018). However, circumstellar interaction, magnetar (Kasen & Bildsten 2010; Woosley 2010) energy input, and black hole accretion (Woosley 1993; MacFadyen & Woosley 1999; Dexter & Kasen 2013) may be important in some cases. A particular subgroup of core-collapse supernovae (SNe) are linked to long-duration gamma-ray bursts (GRBs; these include X-ray flashes, a soft-spectrum variety of GRBs). Although the connection is well established, it is not well understood.

Long-duration GRB-SNe (henceforth, simply GRB-SNe) are all of Type Ic (Filippenko 1997; Woosley & Bloom 2006) – they are produced by stars that have lost their outer hydrogen and helium layers. They are distinct from other SNe Ic in having broad lines (SNe Ic-BL), indicating high kinetic energy (isotropic $E_{\rm kin} \approx 5 \times 10^{52}$ erg), which should be corrected downwards by a factor 3–5 to account for asphericity; Maeda et al. 2002). Those related to classical GRBs (as opposed to X-ray flashes or outbursts) have relatively high luminosities (Mazzali et al. 2014; Lyman et al. 2016;

★ E-mail: chris.ashall24@gmail.com

Prentice et al. 2016, 2019), producing ∼0.3–0.5 $M_\odot$ of ^{56}Ni, whose radioactive decay into ^{56}Co and then ^{56}Fe powers their light curves (Mazzali, Iwamoto & Nomoto 2000; Drout et al. 2011). GRB-SNe are also the most massive SNe Ic. They have typical ejected masses of ∼10 $M_\odot$, suggesting that the progenitor stars had initial masses of 30–50 $M_\odot$ (Iwamoto et al. 1998; Deng et al. 2005; Mazzali et al. 2013). Stars in this mass range can collapse to neutron stars or black holes (Ugliano et al. 2012), but the energy of GRB-SNe is far larger than what the classical neutrino-driven mechanism is likely to achieve (Janka 2012). The source of the high SN $E_{\rm kin}$ is therefore likely to be the compact remnant.

Fewer than a dozen SNe connected with high-energy events (GRBs, X-ray flashes, and outbursts), all at redshift $z < 0.2$, have accurate photometric and spectroscopic time-series (Galama et al. 1998; Hjorth et al. 2003; Matheson et al. 2003; Stanek et al. 2003; Ferrero et al. 2006; Mazzali et al. 2008; Tanaka et al. 2009; Bufano et al. 2012; D'Elia et al. 2015; Toy et al. 2016; Izzo et al. 2019). GRB 161219B (D'Ai et al. 2016), which had an observed isotropic energy in gamma-rays of 1.6×10^{50} erg (Frederiks et al. 2016), exploded on 2016 December 19 (UT dates are used throughout this paper) in a galaxy at $z = 0.1475$ (Tanvir et al. 2016; Cano et al. 2017). About 5 d after the GRB exploded an SN component was detected underlying the optical afterglow. Its spectral features were typical of those of previously observed GRB-SNe, warranting a classification as an SN Ic (Pian, Palazzi & Perley 2016), specifically 'SN Ic-3' (Prentice & Mazzali 2017). Cano et al. (2017) reported the presence of a pre-maximum bump that is reminiscent of the early-time behaviour of other SNe, both accompanied and not accompanied by a GRB. Here we report on optical photometric and spectroscopic follow-up observations of the afterglow of GRB 161219B and the associated SN 2016jca, and compare them with X-ray and ultraviolet (UV) observations made with the Neil Gehrels *Swift* Observatory. We also present radiative-transfer spectral models of the SN.

2 OBSERVATIONS, DATA REDUCTION, AND RESULTS

Optical photometric and spectroscopic observations of the counterpart of GRB 161219B commenced on December 22.08, or 1.99 d after explosion in the rest frame. Thirteen spectra of the point-like optical transient were obtained with the VLT between 1.99 and 268 d (rest frame) after the GRB, and *BVRI* photometry was acquired in various optical filters in the same time interval. The transient was also observed in *BVgri* using IO:O on the 2 m Liverpool Telescope (LT; Steele et al. 2004) and in *BVRI* using the DOLORES camera on the Italian 3.6 m Telescopio Nazionale Galileo (TNG) at Observatorio del Roque de Los Muchachos, Spain. Photometry was also obtained with the Low Resolution Imaging Spectrometer (LRIS; Oke et al. 1995) with the 10m Keck-1 telescope on Maunakea, Hawaii, USA. A log of the photometric and spectroscopic observations can be found in Tables 1 and 2, respectively. In addition, we downloaded the *Swift* XRT data of the GRB counterpart from the archive and re-analysed the *Swift* UVOT observations presented by Cano et al. (2017).

2.1 Optical photometry

Photometric instrumental magnitudes were calculated using aperture photometry through a custom PYTHON pipeline utilizing the IRAF DAOPHOT package. FORS2 photometry was calibrated against secondary photometric standards in the field of view of the target. The local standards have been chosen among isolated stars in regions of constant background, and far away from bright and saturated objects. Their point-spread-function magnitudes were obtained with the same photometric zero point used to calibrate the magnitudes of stars in the Landolt fields SA95 and SA98 observed (respectively) before and after SN 2016jca on the nights of December 22 and 29. The LT photometry was calibrated to stars from the American Association of Variable Star Observers Photometric All-Sky Survey (APASS) Data Release 9. The TNG data reduction, including de-biasing and flat-fielding, was carried out following standard procedures: the cross-calibrated magnitudes were obtained using aperture photometry with respect to the secondary standard stars reported in Table A1 of Appendix A.

To the photometry we applied a Galactic extinction correction using $E(B-V)_{\rm Gal} = 0.028$ mag (Schlafly & Finkbeiner 2011) and the extinction curve of Cardelli, Clayton & Mathis (1989), and as well a K-correction determined from our observed spectra. The resulting *BVRI* light curves are reported in Fig. 1. The detection of the GRB counterpart with all *UVOT* filters and the multiwavelength spectral shape (see the next section) at early epochs suggest that intrinsic absorption due to dust in the host galaxy is negligible, so we have not attempted to evaluate a correction for such an effect.

2.2 Optical spectroscopy

Low-resolution spectra were acquired at the ESO Very Large Telescope (VLT) equipped with the FORS2 spectrograph using a variety of set-ups during the first 3 months after GRB detection (in the photospheric phase). During some of these observations the 300V grism was used and also an order-separating filter was used, owing to severe contamination longwards of 6000 Å by second-order light. These data are complemented with a VLT (plus X-Shooter) spectrum obtained on 2017 October 18 and 23 (see Table 2).

The 2D FORS2 spectral images were flat-fielded and de-biased, and the 1D spectra were optimally extracted (Horne 1986) and reduced following standard procedures within IRAF. They were then linearized and calibrated with respect to catalogued spectrophotometric standards, and corrected for atmospheric extinction. The flux calibration was refined by comparison with the simultaneous broad-band photometry. Telluric absorption lines and weak emission lines from the host galaxy were removed.

Fig. 2 shows the FORS2 spectral sequence after correcting for Galactic reddening and the host-galaxy contribution under the point-like source. Both the wavelength scale and epochs are reported in the host-galaxy rest frame. The most prominent emission lines of the host galaxy have been removed. The afterglow dominates the early emission: at $t = 1.99$ d the spectrum shows the usual afterglow power-law flux distribution, and no SN features are detected. (The low-level undulations are likely to be artefacts of the observation and data-reduction process; Filippenko 1982). The spectrum obtained at $t = 3.73$ d still has a strong afterglow contribution, but it begins to show undulations seen in other GRB-SNe. At $t = 5.52$ d, however, the spectral features typical of previously observed GRB-SNe are clearly seen, and by day 14.20 the observations look like a normal broad-lined SN Ic. The slope of the optical spectrum at ∼2 d, when the SN and host-galaxy contributions are still negligible, is $\beta_{\rm opt} \approx 0.35$.

Simultaneous UV, optical, and near-infrared spectra (∼3000–21 000 Å) were taken with X-shooter using slit widths of 1.0, 0.9, and 0.9 inch, for each arm, respectively (D'Odorico et al. 2006). We used a nodding throw along the slit (nodding lengths of 5 inch) to

Table 1. Log of photometric observations (mag).

MJD	*B*	*V*	*R*	*I*	*g*	*r*	*i*	Telescope
57744.08	19.83 ± 0.01	19.66 ± 0.01	19.39 ± 0.01	18.89 ± 0.00	–	–	–	VLT
57746.08	20.04 ± 0.01	19.84 ± 0.01	19.74 ± 0.01	19.33 ± 0.01	–	–	–	VLT
57748.12	20.24 ± 0.01	19.82 ± 0.01	19.73 ± 0.01	19.48 ± 0.01	–	–	–	VLT
57749.03	20.21 ± 0.03	19.65 ± 0.10	19.53 ± 0.02	19.35 ± 0.05	–	–	–	TNG
57749.99	20.18 ± 0.13	19.8 ± 0.2	–	–	19.81 ± 0.05	19.63 ± 0.07	19.80 ± 0.03	LT
57750.00	–	19.8 ± 0.2	–	–	19.80 ± 0.05	19.63 ± 0.07	19.80 ± 0.03	LT
57751.09	20.46 ± 0.01	19.79 ± 0.01	19.64 ± 0.01	19.44 ± 0.01	–	–	–	VLT
57751.98	–	19.63 ± 0.05	–	–	19.92 ± 0.05	19.54 ± 0.09	19.76 ± 0.08	LT
57751.99	–	19.63 ± 0.05	–	–	19.92 ± 0.05	19.54 ± 0.09	19.75 ± 0.08	LT
57753.99	20.52 ± 0.21	19.77 ± 0.06	19.43 ± 0.06	19.35 ± 0.12	–	–	–	TNG
57754.28	20.57 ± 0.01	19.82 ± 0.01	19.53 ± 0.01	19.40 ± 0.01	–	–	–	VLT
57756.36	20.87 ± 0.01	20.17 ± 0.03	19.64 ± 0.03	19.44 ± 0.04	–	–	–	Keck
57757.00	20.60 ± 0.09	20.2 ± 0.1	–	–	20.28 ± 0.03	19.64 ± 0.03	19.76 ± 0.02	LT
57757.01	20.60 ± 0.09	20.2 ± 0.1	–	–	20.28 ± 0.03	19.64 ± 0.03	19.76 ± 0.02	LT
57757.98	20.90 ± 0.06	20.03 ± 0.03	–	–	20.39 ± 0.04	19.77 ± 0.07	19.76 ± 0.05	LT
57757.98	20.90 ± 0.06	20.03 ± 0.03	–	–	20.38 ± 0.04	19.75 ± 0.08	19.75 ± 0.05	LT
57758.04	20.92 ± 0.02	19.96 ± 0.01	19.58 ± 0.01	19.41 ± 0.01	–	–	–	VLT
57758.96	–	–	–	–	20.44 ± 0.08	19.669 ± 0.08	19.59 ± 0.06	LT
57760.06	21.18 ± 0.02	20.12 ± 0.01	19.66 ± 0.01	19.47 ± 0.01	–	–	–	VLT
57763.26	21.58 ± 0.06	20.33 ± 0.02	19.73 ± 0.01	19.47 ± 0.01	–	–	–	VLT
57767.17	–	20.51 ± 0.03	19.97 ± 0.02	19.61 ± 0.02	–	–	–	VLT
57769.98	–	–	–	–	–	20.35 ± 0.05	20.05 ± 0.02	LT
57770.91	–	–	–	–	–	20.33 ± 0.04	20.11 ± 0.02	LT
57772.04	21.98 ± 0.01	20.93 ± 0.01	20.25 ± 0.01	19.82 ± 0.01	–	–	–	VLT
57772.91	–	–	–	–	–	20.50 ± 0.042	20.22 ± 0.02	LT
57778.88	–	–	–	–	–	20.52 ± 0.07	20.27 ± 0.03	LT
57779.22	22.17 ± 0.02	21.23 ± 0.02	20.56 ± 0.01	20.08 ± 0.01	–	–	–	VLT
57779.92	–	–	–	–	–	20.73 ± 0.03	20.45 ± 0.03	LT
57836.04	22.64 ± 0.03	–	21.24 ± 0.01	–	–	–	–	VLT

Table 2. Log of VLT spectroscopic observations. Note that all spectra were taken at an airmass of about 1.1 and sub-arcsecond seeing, and were acquired at parallctic angle.

Epoch (UT)	Epoch (MJD)	Phase (days[a])	Setup (Instr. + grism)	Range (Å)	Filter	Exp. time (s)
2016 Dec. 22.05	57744.05	1.99	FORS2 + 300V	3300–6600	···	1800
2016 Dec. 24.05	57746.05	3.73	FORS2 + 300V	3300–6600	···	1800
2016 Dec. 26.10	57748.10	5.52	FORS2 + 600B	3300–6200	···	1800
2016 Dec. 29.07	57751.07	8.10	FORS2 + 300V	4000–8650	gg435[b]	1800
2017 Jan. 01.26	57754.26	10.89	FORS2 + 300V	4000–8650	gg435	1800
2017 Jan. 05.06	57758.06	14.20	FORS2 + 300V	4000–8650	gg435	1800
2017 Jan. 07.08	57760.08	15.96	FORS2 + 600B	3300–6200	···	1800
2017 Jan. 10.24	57763.24	18.71	FORS2 + 300V	3300–6600	···	1800
2017 Jan. 14.15	57767.15	22.12	FORS2 + 300V	4000–8650	gg435	1800
2017 Jan. 26.24	57779.24	32.65	FORS2 + 300V	4000–8650	gg435	1800
2017 Mar. 23.43	57835.43	81.69	FORS2 + 300V	4000–8650	gg435	2400
2017 Oct. 18.27	58044.23	263.58	X-Shooter	3000–22,000	···	4200
2017 Oct. 23.27	58049.23	267.93	X-Shooter	3000–22,000	···	4200

[a]Rest frame.
[b]Order separator.

obtain better sky subtraction. The data were reduced using version xshoo/2.7.0b of the ESO X-shooter pipeline (Modigliani et al. 2010) with the calibration frames (biases, darks, arc lamps, and flat fields) taken during daytime. The spectra were extracted using standard IRAF tasks. Spectrophotometric and telluric standard star exposures taken on the same night as SN 2016jca observations were used to flux-calibrate the spectra and to remove telluric features. The X-shooter spectra were co-added to improve the signal-to-noise ratio.

The average spectrum, cleaned of artefacts, and spurious emission features, are shown in Fig. 3. Since at this late epoch, +267 d, the SN spectrum should be dominated by nebular line emission, while the afterglow emission has completely faded, the spectral continuum is entirely due to the host galaxy, as confirmed by comparison with the archival Pan-STARRS photometry. Lack of detection of the nebular [O I] λλ6360, 6363 emission line (the strongest line typically detected at this late phase) leads to a 3σ upper limit

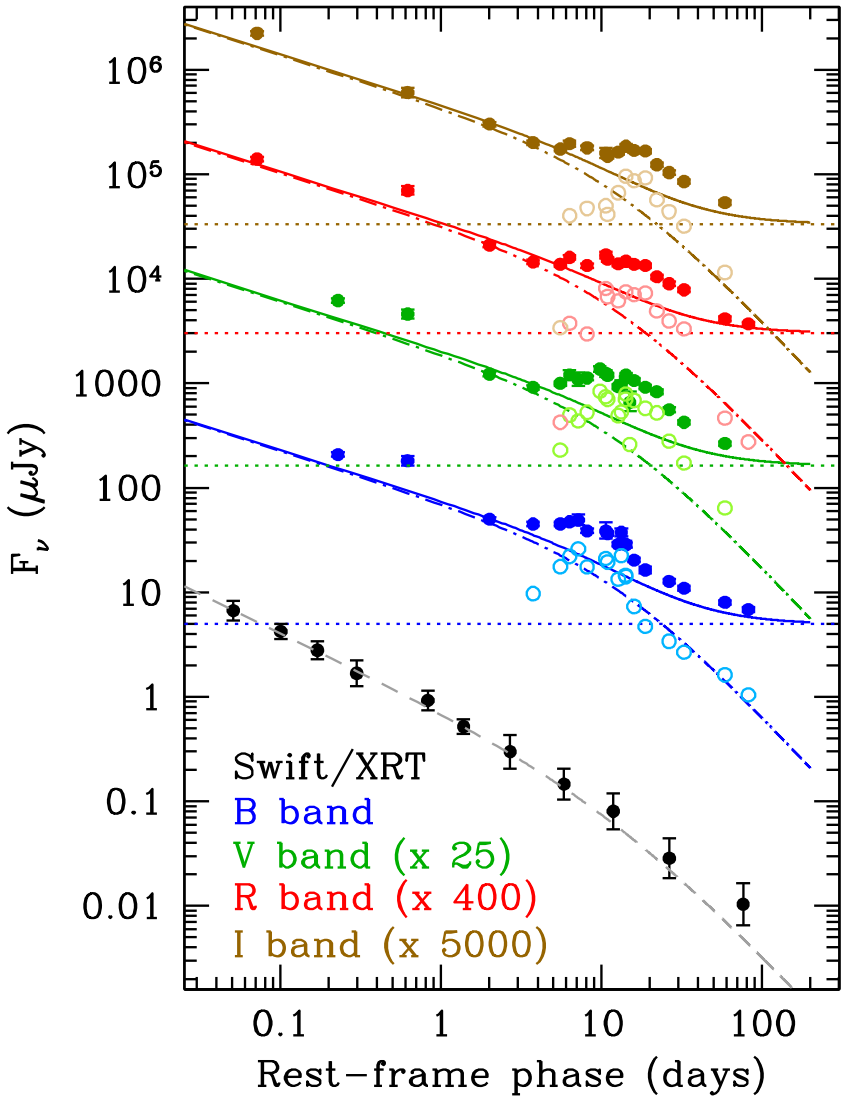

Figure 1. Multiwavelength light curves of the GRB 161219B counterpart. The optical light curves in *BVRI* filters (filled circles), constructed based on our and literature data, are K-corrected and deabsorbed for Galactic extinction. The dotted horizontal line in each panel represents the host-galaxy contribution in that band; the dot-dashed curves represent the afterglow modelled with a steepening power law (see the text). The solid curve is the sum of the afterglow and host-galaxy components. The subtraction of these two components from the observed points corresponds to the SN light curves in *BVRI* bands (light blue, light green, pink, and beige open circles, respectively). The errors on the SN points are not reported for clarity and range from 10 to 15 per cent around maximum to 50 per cent at early epochs, when the contribution of the afterglow is larger. The black filled circles are the *Swift*/XRT light curve at 1 keV; the best-fitting afterglow model is reported as a grey dashed curve.

of $\sim 10^{-16}$ erg s^{-1} cm^{-2} on its intensity, corresponding to a line luminosity of $\sim 10^{40}$ erg s^{-1}. Additional late-time spectroscopy was also conducted at the 10.4 m GTC (+ OSIRIS) on 2017 January 17.

2.3 X-ray and ultraviolet data

Mingo et al. (2016) provide a preliminary report on the *Swift*/XRT (0.3–10 keV) observations of GRB 161219B. The spectrum and light curve were downloaded from the *Swift* archive (http://www.swift.ac.uk/xrt_spectra/ and http://www.swift.ac.uk/xrt_curves). Once corrected for Galactic ($N_{\rm HI} = 3.06 \times 10^{20}$ cm^{-2}) and intrinsic ($N_{\rm HI} = (1.5 \pm 0.2) \times 10^{21}$ cm^{-2}) neutral hydrogen absorption, the X-ray spectrum is described by a single power law $f(\nu) \propto \nu^{-\beta_{\rm X}}$, $\beta_{\rm X} = 0.83 \pm 0.06$ (the uncertainty is 90 per cent confidence). Using this spectral slope, we have converted the X-ray fluxes into monochromatic fluxes at 1 keV (Fig. 1).

The *Swift*/UVOT began observing the field of GRB 161219B 92 s after the *Swift*/BAT trigger. Observations were taken in both image and event modes. The afterglow was detected in all seven *UVOT* filters. Before extracting count rates from the event lists, the astrometry was refined following the methodology of Oates et al. (2009). The source counts were extracted initially using a source region of 5 arcsec radius. When the count rate dropped to below 0.5 counts per second, we used a source region of 3 arcsec radius. In order to be consistent with the UVOT calibration, these count rates were then corrected to 5 arcsec using the curve of growth contained in the calibration files. As the afterglow is situated at the edge of the halo of a bright star, we used several small circular regions at a similar distance around the halo in order to extract the background counts. The count rates were obtained from the event and image lists

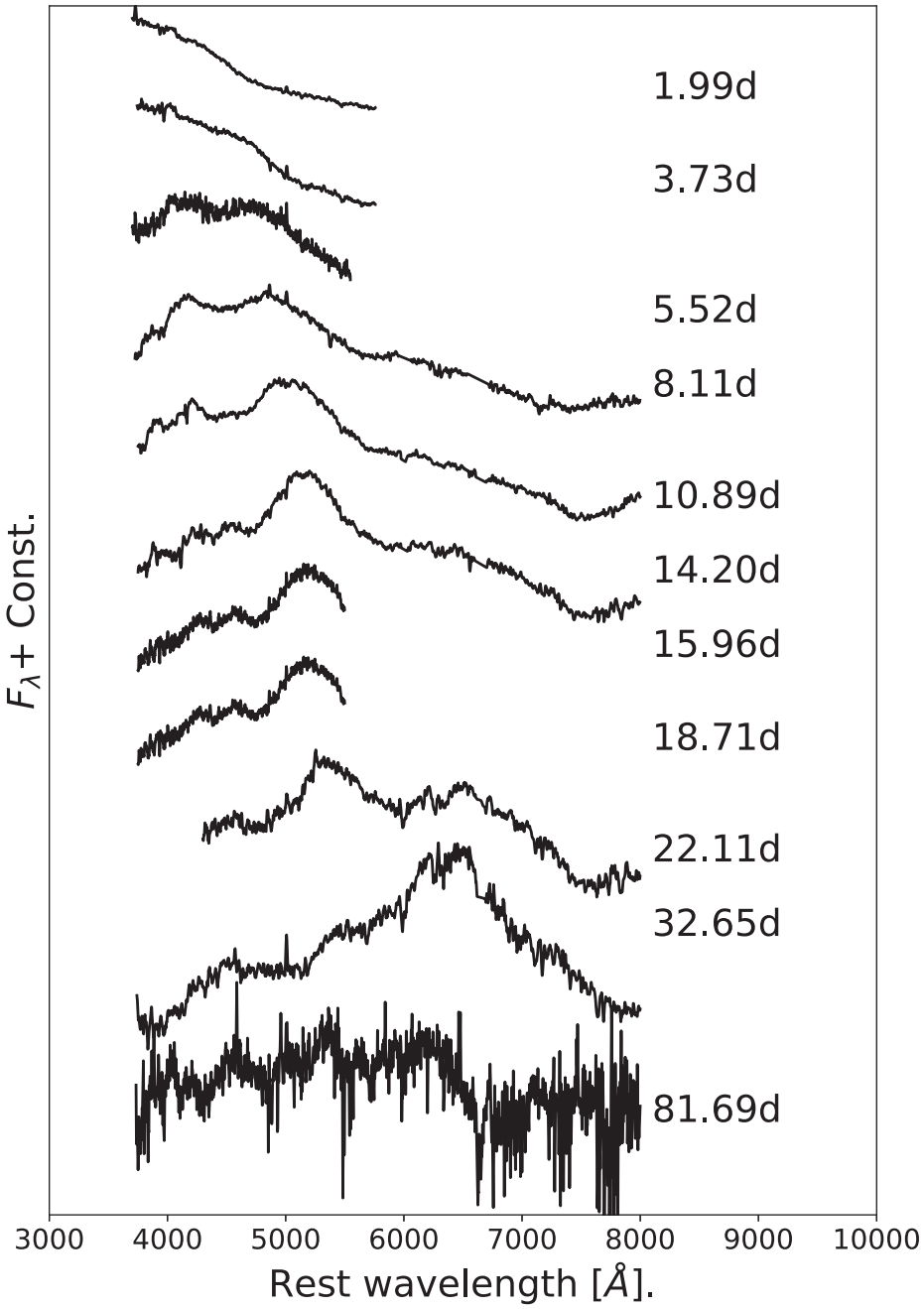

Figure 2. A temporal series of spectra of the transient. The time (in the rest frame) from explosion, *t*, is given for all spectra. The spectra are in the rest frame, corrected for foreground Galactic extinction and host-galaxy subtracted. This first spectrum appears to have no contribution from the SN component.

using the *Swift* tools `uvotevtlc` and `uvotsource`, respectively. They were converted to magnitudes using the UVOT photometric zero points (Poole et al. 2008; Breeveld et al. 2011). The UVOT data, dereddened using the same procedure followed for the optical data, are shown in Fig. 4. The analysis pipeline used software HEADAS 6.19 and UVOT calibration 20150717. To improve the signal-to-noise ratio, the count rates in each filter were binned using $\Delta t/t = 0.2$; this effectively bins only the late-time exposures.

The settling image is generally excluded as it may be affected by changes in the cathode voltage during the first few seconds. We compared the magnitudes of several stars in the settling image with later images and do not find a systematic difference; we therefore include this exposure in our analysis.

2.4 Decomposition of the multiwavelength light curves and spectra

In order to study the SN component of the GRB optical counterpart, we must first subtract the contribution of the host galaxy and afterglow from the light curves and spectra of SN 2016jca. The host galaxy is clearly detected and resolved in both the VLT images and a *Hubble Space Telescope (HST)* image taken with WFC3/UVIS and

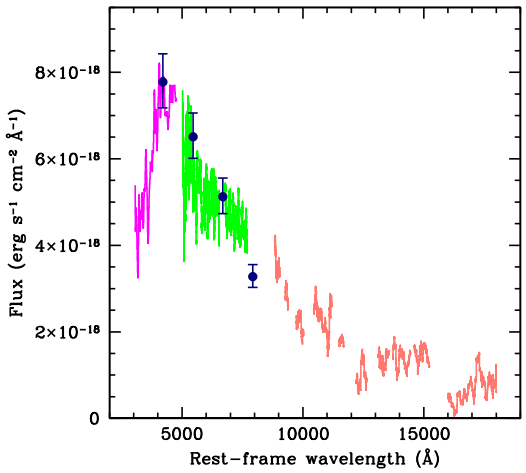

Figure 3. VLT X-Shooter spectrum obtained from the average of observations taken on 2017 October 18 and 23, with the near-UV (magenta), optical (green), and near-IR (orange) arms. The spectrum is corrected for redshift and Galactic extinction and cleaned for artefacts and spurious features. The dark-blue points indicate the extinction-corrected Pan-STARRS photometry of the host galaxy. They are consistent with the spectral continuum, indicating that the latter is dominated by the host emission, with no evidence of nebular emission lines due to the SN. It is apparent from the spectrum that there is no sign of the SN at this epoch, +265 d.

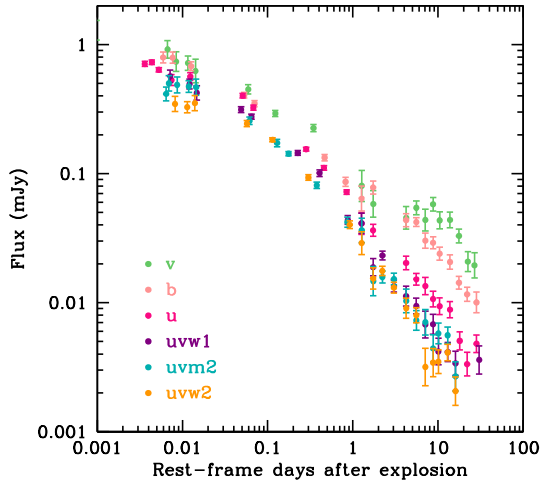

Figure 4. UVOT light curves in six filters corrected for Galactic extinction.

the open LP filter (about 2000–10 000 Å); see Cano et al. (2017). We have identified on archival Pan-STARRS images of the host the precise position of the GRB-SN and have measured the flux of the host within a circle of 1 arcsec radius. The *griz* apparent magnitudes are $g = 23.0 \pm 0.1$, $r = 22.6 \pm 0.1$, $i = 22.4 \pm 0.1$, and $z = 22.5 \pm 0.1$. The resulting colours are typical of a modestly absorbed star-forming galaxy (Kinney et al. 1996). We have converted these magnitudes to the Bessel *BVRI* system for subtraction from the optical counterpart.

While the initial temporal decline of the GRB optical counterpart can be attributed to a monotonically decreasing afterglow formed in a blast wave, starting around day 2–3 all light curves show a rebrightening. We interpret this as SN emission, as clearly confirmed by the spectra that exhibit the typical stripped-envelope SN signature, especially at late times when the afterglow negligibly contributes to the total flux.

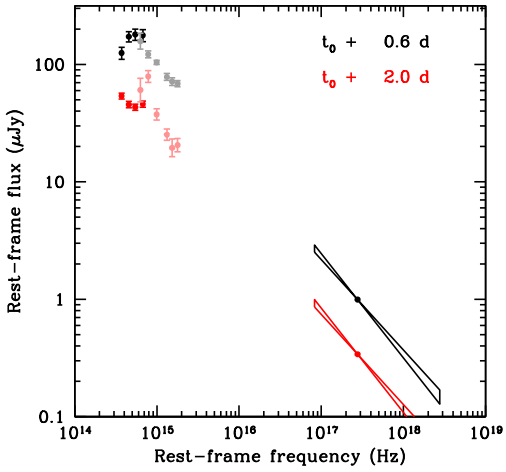

Figure 5. SEDs of the GRB counterpart at 0.62 (black) and 2 (red) rest-frame days after explosion, corrected for Galactic and (for X-rays only) intrinsic extinction. The optical data at the first epoch are from the literature, while at the second epoch they represent our VLT FORS2 photometry. The simultaneous UVOT data are also reported in lighter shades (grey for $t_0 + 0.62$ d and pink for $t_0 + 2$ d). The X-ray data are power-law spectral fits with index $\beta_X = 0.83 \pm 0.06$. The host galaxy and SN flux are negligible with respect to the optical afterglow at these epochs and thus are not subtracted from the optical data. The optical magnitudes were converted to fluxes using the zeropoints from Fukugita, Shimasaku & Ichikawa (1995).

The afterglow contribution was estimated as follows. We first constructed optical-to-X-ray spectral energy distributions (SEDs) at 0.62 and 2 rest-frame days. This corresponds to the first epoch that *BVRI* photometry was reported and to the epoch of our first VLT/FORS spectrum, respectively. The SEDs are plotted in Fig. 5. The data are corrected for Galactic extinction, and in the X-ray band also for intrinsic extinction. At these early epochs, the host-galaxy contribution is negligible. The SEDs and the spectral indices estimated above in the individual domains ($\beta_{opt} \approx 0.35$, $\beta_X = 0.83 \pm 0.06$) show that the optical broad-band spectrum has a significantly flatter slope than the X-ray spectrum and suggests that a cooling frequency, ν_c (Sari, Piran & Narayan 1998), is between the optical and X-ray bands at these two epochs ($\sim 10^{15}$ Hz). If the X-rays are produced by synchrotron radiation, this implies that the electron energy distribution, $dN/d\gamma \propto \gamma^{-p}$, must have a slope $p = 2 \times \beta_X = 1.66 \pm 0.12$ (Sari et al. 1998; Zhang, Woosley & Heger 2004). This corresponds to an optical spectral index $\beta_{opt} = (p - 1)/2 = 0.36$, in agreement with the spectral slope measured in the *BVRI* wavelength range.

Although the X-ray light curve shows a deviation from a power law in the form of temporal steepening (see Fig. 1), it can be formally fitted with a single power law, $t^{-\alpha_X}$, with $\alpha_X = 0.88 \pm 0.05$. According to standard fireball theory, the optical light curve should then decay with $\alpha_{opt} \approx 0.63$. However, this not only overpredicts the flux at epochs later than $\sim$20 d, but the residuals prior to day $\sim$20 can only be accounted for by an SN that is a factor of 10–30 less luminous than SN 1998bw. This is inconsistent with the spectra of SN 2016jca that are approximately similar, at all epochs from few days to 3 months after explosion, to those of SN 1998bw at comparable phases, implying that the temperature conditions (and therefore the luminosities) in the two SNe must be comparable (see Fig. 7). Hence, the temporal modelling of the multiwavelength afterglow must account for some steepening, that we ascribe to an

achromatic break in the transition from a spherical expansion of the plasma to a jet geometry (Rhoads 1999; Sari, Piran & Halpern 1999)

For $\nu > \nu_c$ and $p = 1.66$, the standard fireball theory of a relativistic shock propagating spherically in a constant-density circumstellar medium prescribes that $\alpha = (3p + 10)/16 = 0.95$ ('flat electron spectrum' scenario, with $p < 2$; Dai & Cheng 2001; Zhang et al. 2004). However, this is significantly steeper than our early measured X-ray decay rate. On the other hand, by applying the 'classical' steep electron spectrum scenario valid for $p > 2$, we predict $\alpha = (3p - 2)/4 = 0.75$, which is more consistent with observations.

Therefore, we have a contradiction whereby, although the X-ray spectrum constrains p to be less than 2, the X-ray light curve is consistent with fireball theory only for a scenario where $p > 2$. In order to solve this discrepancy, we conclude that either a standard impulsive blast-wave model is inapplicable in this case, or that the shallow decay is due to a continuous, rather than impulsive, energy injection from the central engine to the blast wave, which slows down the decay. Since fireball theory appears to be a good description of the multiwavelength afterglow (see below), we assume that the latter hypothesis is more likely and postulate that the shock undergoes a re-energization episode whereby, starting ~0.1d after the explosion (i.e. before the epoch of the first SED; see Fig. 5), energy in the form $L(t) \propto t^{-q}$ is injected in the fireball.

In a spherical geometry, uniform-density medium and flat electron spectrum ($p < 2$) scenario, the expected time-decay index is $\alpha = [(2 + q)p + 18q - 12]/16$ below the cooling frequency (i.e. the optical spectral range; see full derivation in Appendix A). Note that, for $p = 1.66$ and $\alpha_{opt} \approx 0.5$, we have $q \approx 0.85$. Since $q < 1$, the blast-wave energy increases in time and it reduces the decay rates, as observed. Above the cooling frequency (X-ray band), the above p and q parameters imply a decrease rate of $t^{-0.8}$, consistent with the observed early-time decay of the X-ray light curve. At late epochs, the predicted time-decay index in optical and X-rays is $\alpha_2 = p = 1.66$.

Then we determined the lower and upper boundaries of the achromatic break time of the light-curve power-law decay. We adopted the temporal double power-law model of Israel et al. (1999), and studied the X-ray light curve, that does not contain a significant SN component and is exclusively due to synchrotron emission (any host galaxy component must also be negligible at the observed X-ray flux levels).

After fixing the electron slope to $p = 1.66$, we stepped the break time from 1 to 30 d, with a 1 d increase at each iteration. For each value of the break time, we explored 100 values of the flux normalization, stepped in a range that was iteratively adjusted until a χ^2 minimum was found. The formal best-fitting break time is 26 d, with a lower boundary of 13 d, determined following Avni (1976). However, for a break time of 26 d or larger, the luminosity of the SN resulting from the afterglow subtraction (see below) is incompatible with the temperature that is necessary to describe the spectra. For example, in spectral models of the SN, for these late break times, to keep the temperature and ionization state constant in the models, the photospheric velocity would have to increase from day 3.73 to 5.52, which is unphysical. For a break time of 13 d the model is compatible with the latest X-ray point lower boundary, and also returns an acceptable SN luminosity after subtraction. Our best estimate of the break time is $t_b = 13 \pm 2$ d. An afterglow model was constructed based on the above parameters ($p = 1.66$, $t_b = 13$ d, cooling frequency at 0.6 d after explosion $\nu_C = 1.6 \times 10^{15}$ Hz, flux at ν_C during t_b $f_\nu = 6.2$ μJy) and on fireball theory.

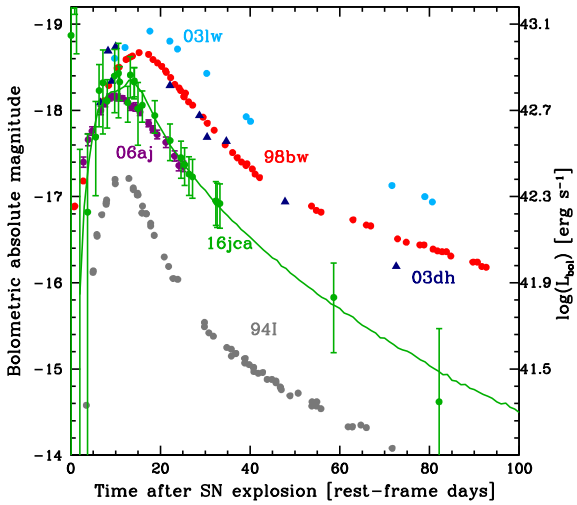

Figure 6. Pseudobolometric light curve (3000–10 000 Å) of SN 2016jca after the subtraction of the host galaxy and afterglow components, compared with bolometric light curves of previous GRB-SNe 1998bw, 2003dh, 2003lw, and X-ray flash SN 2006aj (Galama et al. 1998; Malesani et al. 2004; Deng et al. 2005; Pian et al. 2006), and the 'normal' Type Ic SN 1994I (not associated with a GRB) (Richmond et al. 1996). Note the similarity with the light curve of SN 2006aj. To avoid confusion, the error bars are shown only for SN 2016jca. The uncertainties of SN 1998bw are smaller than the markers, SN 2006aj are ~10 per cent, and SN 2003dh and SN 2003lw are comparable to those of SN 2016jca. The first points, as in SN 2003dh, are heavily contaminated by the afterglow. The solid green line is the model light curve produced with the density and abundance structure used for the spectra modelling.

If the achromatic time break is related to the presence of a homogeneous jet where the plasma expands, we estimate its full opening angle to be $\theta = 42° \pm 3°$ (Sari et al. 1999), assuming a medium density of 1 cm^{-3} and the observed isotropic energy of 1.6×10^{50} erg (Frederiks et al. 2016).

We stress that the re-energization of the blast wave, postulated to slow down the decay rates of the observed light curves, does not add any degree of freedom to the χ^2 evaluation, its power-law index q being determined univocally by the value of p and being physically acceptable as long as it is <1.

By subtracting from the observed *BVRI* light curves the constant host-galaxy flux and the afterglow component in each band as derived from our multiband fit using a break time of 13 d, we obtained the *BVRI* light curves of SN 2016jca. These were used to construct, following a procedure similar to that adopted by Mazzali et al. (2017), a bolometric light curve in the range 3000–10 000 Å, which is plotted in Fig. 6.

Similarly, we subtracted the host and the afterglow *BVRI* SEDs from every dereddened and deredshifted spectrum of SN 2016jca and used these decomposed spectra for comparison with SN models (see Section 4).

3 THE SUPERNOVA COMPONENT

The peak of the bolometric light curve of SN 2016jca (see Fig. 6) occurred at 10 ± 2 d after the GRB, at −18.2 ± 0.1 mag. A ^{56}Ni mass of ~0.27 ± 0.05 $M_\odot$ is required to power the luminosity of the light curve if it is due to radioactivity, as is seen from the model in Fig. 6. This ^{56}Ni mass is similar to those of most other well-observed GRB-SNe. However, the rise time is shorter than that of other GRB-SNe by ~2 d, and significantly shorter than the

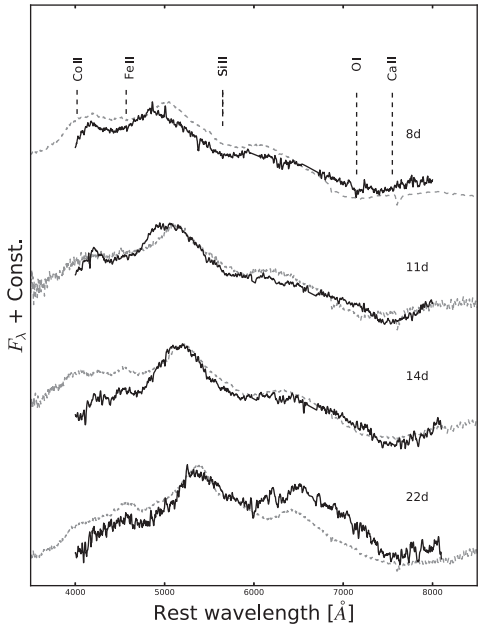

Figure 7. Spectra of SN 2016jca (black) and SN 1998bw (grey dotted) (Iwamoto et al. 1998) at $t = 8$, 11, 14, and 22 rest-frame days after explosion. The spectra are in the rest frame, corrected for Galactic extinction ($E(B-V)_{\rm Gal} = 0.028$ and 0.052 mag, respectively) and host-galaxy subtracted.

prototypical GRB-SN, SN 1998bw. This may indicate that the ejecta mass of SN 2016jca is smaller than SN 1998bw, or it may imply that the viewing angle to the SN symmetry axis is different, or that there is a larger abundance of ^{56}Ni located further out in the ejecta in SN 2016jca, or a combination of all three.

Spectroscopically, SN 2016jca has the standard broad absorption features attributed to GRB-SNe. These are Fe II absorption at ∼4200 Å, Si II absorption at 5800 Å, and the O I/Ca II feature at 7600 Å. The broad absorption features in GRB-SNe are caused by a larger line-forming region compared to standard SNe Ic. This larger region requires there to be sufficient densities at high velocities well above the photosphere to produce opacity. Therefore, SNe with broader features have shallower density profiles (Mazzali et al. 2017). In effect, the gradient of the outer density profile of the ejecta determines the breadth of the lines: shallower profiles produce broader lines. Hence, SNe with high specific $E_{\rm kin}$ have broader lines. Spectroscopically SN 2016jca is similar to SN 1998bw, but SN 2016jca has more absorption in the blue (see Fig. 7). This increased absorption is likely to be due to a higher abundance of Fe group elements in SN 2016jca, and we test this hypothesis below.

4 SPECTRAL MODELS

4.1 The code

Having determined the afterglow properties and isolating the SN component, we now turn to spectral modelling to analyse SN 2016jca. We use a 1D Monte Carlo radiative-transfer code, which follows the propagation of photon packets through an SN atmosphere, to produce synthetic spectra. The code is based on work presented by Mazzali & Lucy (1993), Lucy (1999) and Mazzali et al. (2000). This technique utilizes the fact that as time passes, progressively deeper layers of the SN ejecta can be seen, since an SN can be assumed to be in homologous expansion starting ∼10 s after explosion. We have $r = v_{\rm ph} t_{\rm exp}$, where r is the distance from the centre of the explosion, $v_{\rm ph}$ is the photospheric velocity, and $t_{\rm exp}$ is the time from explosion. The Schuster–Schwarzschild approximation is used, which assumes that the radiative energy is emitted at an inner boundary in the form of a black body. This is a sound approximation for modelling a GRB-SN, as it yields good results, owing to the amount of material above the photosphere. Furthermore, the approximation does not require in-depth knowledge about the radiation transport below the photosphere.

The code has previously been successfully used for Type Ia SNe (e.g. Ashall et al. 2014, 2016, 2018) as well as core-collapse SNe (e.g. Mazzali et al. 2017; Prentice et al. 2018). A detailed explanation of the modelling procedure as well as the error analysis can be found in the companion paper (Ashall & Mazzali 2019). In short, the purpose of the code is to produce optimally fitting synthetic spectra. This is done by varying input parameters, such as the bolometric luminosity, $v_{\rm ph}$, and abundances, given a fixed input density profile. While using a 1D code to infer the structure of the event represents an inherent limitation for the characterization of certain properties such as asymmetry, a higher dimensional code requires that a very large set of assumptions (e.g. asphericity in density/velocity, orientation) must be made, such that it may be very difficult (if not impossible) to distinguish between different options. The approach using a 1D code removes most of these assumptions and allows us to at least get a direct glimpse of one of the most likely reasons for the behaviour of the spectra.

The mass we obtained for SN 2016jca was lower than that for SN 1998bw, as SN 2016jca has a more rapidly evolving light curve. The ejecta mass and $E_{\rm kin}$ of the density profile used were 6.5 $M_\odot$ and 4×10^{52} erg (respectively), although the formal values we adopt for the analysis are $6.5 \pm 1.5\,M_\odot$ with a range of $E_{\rm kin}$ of (3.0–5.0) $\times$ 10^{52} erg. In the modelling procedure, we used constant abundances as a function of velocity, and our most abundant elements are O(∼70 per cent), Ne(∼20 per cent), and C(∼7 per cent), followed by Si(∼1.5 per cent), S(∼0.5 per cent), and ^{56}Ni(∼0.4 per cent), with the remaining 0.5 per cent consisting of Mg, Ca, Fe, and Ti + Cr.

However, having a constant mass fraction of ^{56}Ni as a function of velocity is difficult to reconcile with an aspherical explosion, especially if the ^{56}Ni is produced on the side of the GRB-jet. It would be expected that as the photosphere recedes, the jet, and the heavily synthesized region surrounding the jet, becomes a smaller overall fraction of the total observed region. Therefore, if the ^{56}Ni was produced in the region surrounding the jet it could be expected that its abundance decreases as a function of decreasing velocity. Thus, we test models where the ^{56}Ni abundance changes (both increasing and decreasing) as a function of velocity. Fig. 8 presents the models, as well as models with a flat ^{56}Ni distribution. The (green) model where the ^{56}Ni abundance increases as a function of decreasing velocity produces poor fits. At early times (5.5, 8.1, and 10.9 d) there is not enough blocking by Ni II and Co II lines, owing to their low abundance. Conversely, at later times (22.12 d) there is too much absorption at ∼4200 Å, caused by the decay of ^{56}Ni. The (blue) models with constant ^{56}Ni abundance of 0.4 per cent produce good fits throughout, but the (red) models where the ^{56}Ni abundance decreases as a function of decreasing velocity produce fits which are better or as good as the blue models.

Therefore, we have a range of possible ^{56}Ni values between the red and blue models which produce good fits. These are shown in Fig. 9; the shaded region shows the uncertainty of the ^{56}Ni abundance. There is evidence that the ^{56}Ni abundance decreases as the velocity decreases. This could be explained if an aspherical explosion placed heavy elements in and around the region where

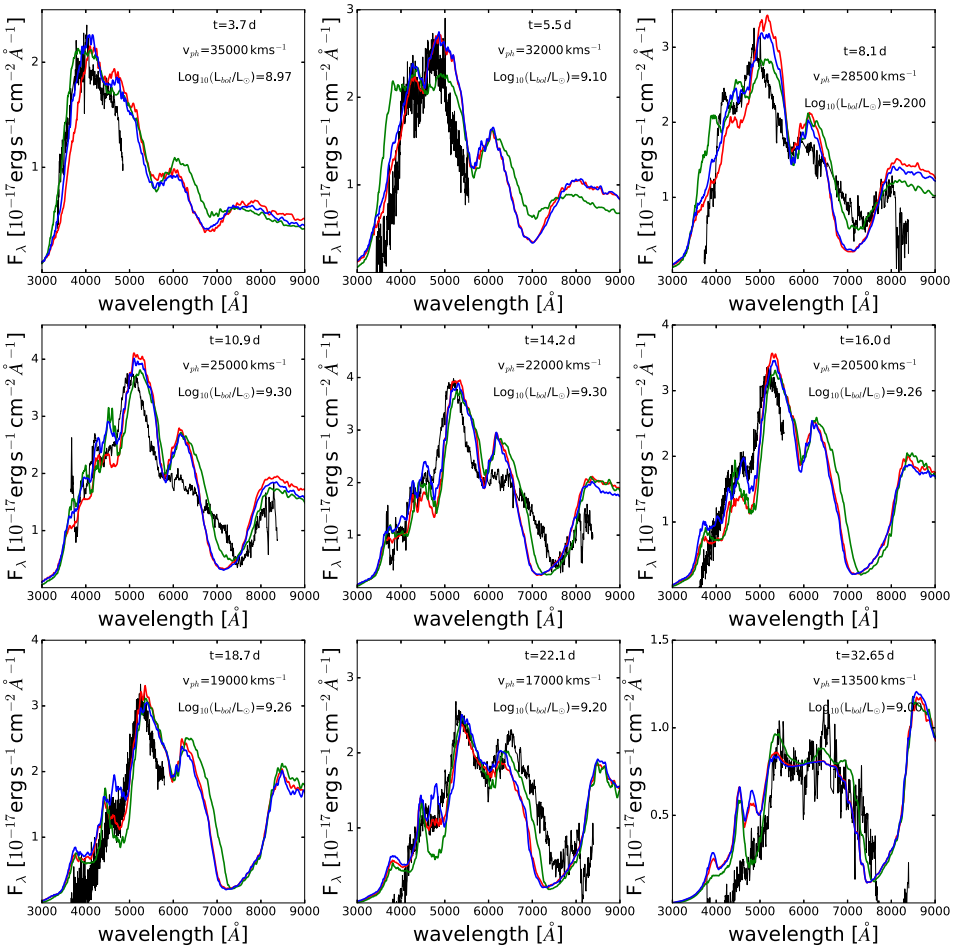

Figure 8. Spectral models produced with ^{56}Ni abundances. The best-fitting blue model has a ^{56}Ni abundance of ∼0.4 per cent, or a ^{56}Ni mass fraction $X_{\rm Ni}$ of 0.004; note that this is the mass fraction relative to the total ejected mass. The red model has a ^{56}Ni abundance which decreases as velocity decreases, and the green model has the opposite trend.

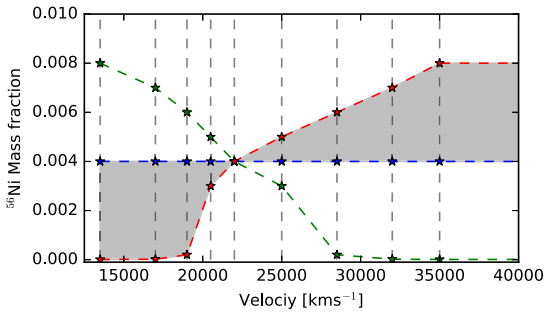

Figure 9. The ^{56}Ni abundance distribution as a function of velocity for the three models presented in Fig. 8. The values of ^{56}Ni which produce good fits are highlighted in grey. The dashed vertical lines represent the photospheric velocity from the nine spectral models. Note that this is the mass fraction relative to the total ejected mass.

the explosion is more energetic. At the earliest epochs, the observed photosphere would consist of more metal-rich material at the highest velocities, and as the photosphere recedes the abundance of lighter material on the side of the ejecta would increase; an example of this can be seen in Fig. 10, and the metal abundance decreases. This could be an indirect evidence that the SN is aspherical both in shape and in elemental distribution.

4.2 Best models

Fig. 11 presents our optimized models; they were produced with the input parameters given in Table 3. The earliest model at 3.7 d is very blue, hot, and almost featureless. Absorption and reprocessing of blue flux is caused by blends of metal lines including Ni II λλ3465, 3471, 3513, 3576, 4067, Co II λλ3388, 3415, 3446, as well as Mg II λλ2795, 2802 resonance lines and Ca II λλ3934, 3969. The model at this early epoch has weak Si II λλ6347, 6371 absorption at 5300 Å, and O I λλ7772, 7774, 7775 and Ca II λλ8498, 8542, 8662 absorption at ∼6500 Å. At this epoch the Sobelov optical depths of the Ca II lines are a fifth of the corresponding O I lines.

Conversely, ∼2 d later at 5.5 d, the model spectrum contains stronger features typically associated with broad-line SNe Ic. The blue region is still depressed in flux owing to line blanketing caused by blends of metal lines, and the absorption at 4200 Å is produced by Fe IIλλ5018, 5169 with some contribution from Si II λ5056. The Ca II near-infrared triplet absorption is stronger than in the previous epoch, and it occurs redwards of the corresponding O I absorption. This is unlike in SN 1998bw, where the Ca II absorption is at shorter wavelengths and higher velocities than that of the O I lines. The

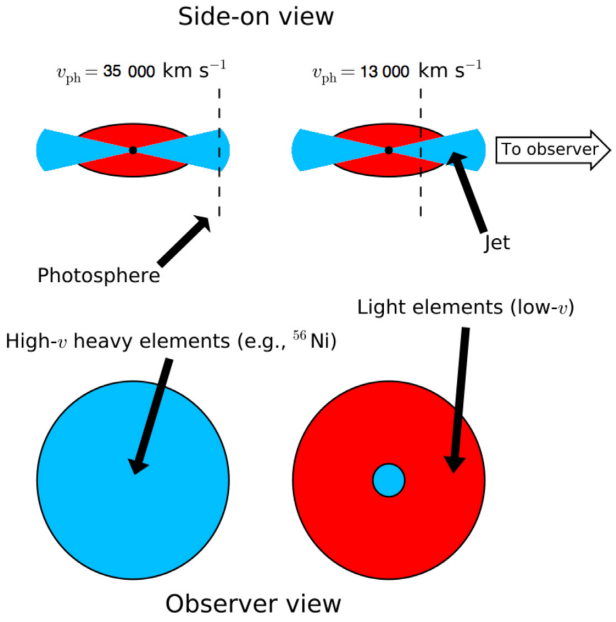

Figure 10. A demonstration of the ejecta velocity distribution in an aspherical explosion with jet component and the dependence on photospheric velocity v_{ph} for spectral line velocities. All material to the left of the photosphere is optically thick to the observer, while material to the right is optically thin; this is where line formation occurs. (Left) At $v_{ph} = 43\,000\,km\,s^{-1}$, the photosphere forms inside the jet, and so only high-velocity material contributes to spectral line formation. (Right) At a lower v_{ph} the photosphere forms across both the high- and low-velocity material, providing a range of line velocities in the spectra. The figure is for illustrative purposes only.

degree of blending in SN 2016jca indicates that the mass above 0.1c is significant, and our models show Ca II absorption up to 0.25c.

As time passes the SN ejecta expand and cool, but increase in luminosity. The peak in bolometric luminosity in the models is reached between the 10.9 and 14.2 d; this coincides with the bolometric maximum derived from the light curve at ∼12 d (see Fig. 6). The models match the observations well at all epochs.

Our models have 0.5 $M_\odot$ of material above 0.1c (of which 2×10^{-3} $M_\odot$ is ^{56}Ni) and 0.1 $M_\odot$ of material (of which 4×10^{-4} $M_\odot$ is ^{56}Ni) above 0.15c. The presence of this mass at such high velocities may represent a connection with the relativistic outflow (Piran et al. 2017). These values should be reduced to take into account the likely asphericity of the SN ejecta, with equatorial material carrying less E_{kin}. Regardless of this, the mass of ^{56}Ni at high velocity is much less than what is required to drive the light curve (∼0.27 ± 0.05 $M_\odot$), and as there is ∼0.03 $M_\odot$ of ^{56}Ni above 10 000 km s^{-1}, we conclude that most of the ^{56}Ni (∼0.24 $M_\odot$) must be located at lower velocities. This ^{56}Ni can efficiently deposit its decay products (gamma-rays and positrons) at advanced epochs and power the spectrum during the nebular phase (∼200 d after explosion). Creating ^{56}Ni at low velocities poses a challenge to GRB-SN models.

4.3 Velocities

Fig. 12 presents the photospheric velocity evolution as a function of time for 12 stripped-envelope SNe. Our comparison of photospheric velocities is based only upon quantities determined with the aid of a spectral model. We do not consider velocities measured from the observed spectra, as these have several drawbacks: observed absorption lines from above the photosphere, and therefore indicate velocities higher than the photospheric velocity and which depend on the strength of the lines. Additionally, lines are usually blended, especially if broad, making it difficult or impossible to isolate the contribution of individual atomic species.

It can be seen in Fig. 12 that the velocity of the photosphere drops rapidly over the first 5 d. SN 2016jca was observed as early as SN 2002ap (Mazzali et al. 2002); however, it shows much higher velocities. The velocity of SN 2016jca at 3.73 d was 35 000 ± 7000 km s^{-1}, and this is the largest photospheric velocity recorded for a GRB-SN. At later times, SN 2016jca evolves like other GRB-SNe, which highlights the similarity among these events as well as their exceptionally high energies. With the exception of SN 2010ah there is a clear difference in the velocity evolution of GRB-SNe and other striped envelope SNe (including those associated with X-ray flashes). GRB-SNe have consistently higher photospheric velocities than standard events, and this trend is also seen with their E_{kin}.

SN 2010bh was previously interpreted as the highest velocity GRB-SN ever discovered. However, in most observational papers velocities are obtained by measuring the minima of a feature – yet as we discussed above, using one transition as a proxy is extremely uncertain. Bufano et al. (2012) find that for SN 2010bh, at 2.4 d after explosion, there is Ca II absorption at ∼47 000 km s^{-1}. If we follow the same approach, measuring the minimum of the feature of our synthetic spectra, we obtain a velocity of ∼71 700 km s^{-1}. Furthermore, if we take a direct measurement from the observed spectra at 8.1 d, the minimum of the O/Ca absorption feature is at ∼7200 Å, which corresponds to a velocity of 47 000 km s^{-1}. This value is the same as that in Bufano et al. (2012) but measured 5 d later, which indicates that the earlier velocities in SN 2016jca must be larger. We note that Toy et al. (2016) present a spectrum of SN 2013dx (which has been afterglow subtracted) at 3.25 d, but their spectra is too noisy for a velocity measurement, with their first measurement being at 9.3 d. In this work we use radiative-transfer models to consistently calculate the photospheric velocity and compare this to other models made with the same radiative-transfer code, which allows for consistency. However, as shown above, if we use the same measuring techniques as in other papers, SN 2016jca still has the highest velocity features.

4.4 Model light curve

To check our results and to verify the density profile and abundance structure we have used in our analysis, we have produced a model light curve. We use a Monte Carlo light-curve code that was first presented by Cappellaro et al. (1997) and expanded by Mazzali et al. (2000). Using the density profile and abundance structure from our best-fitting spectral model, a light curve is produced. The model light curve can be found in Fig. 6; it provides a good fit to the bolometric light curve of SN 2016jca, demonstrating that our density profile, ejecta mass, and E_{kin} are consistent with both the light curve and spectral properties of the SN. It confirms that the ^{56}Ni mass produced in the explosion was 0.27 $M_\odot$, and therefore ^{56}Ni decay was luminous enough to power the light curve. The model light curve predicts that the observed bolometric magnitude of the SN would be 28 mag at day + 265, when the spectrum of the host galaxy was obtained. The ejecta of the SN at this time will

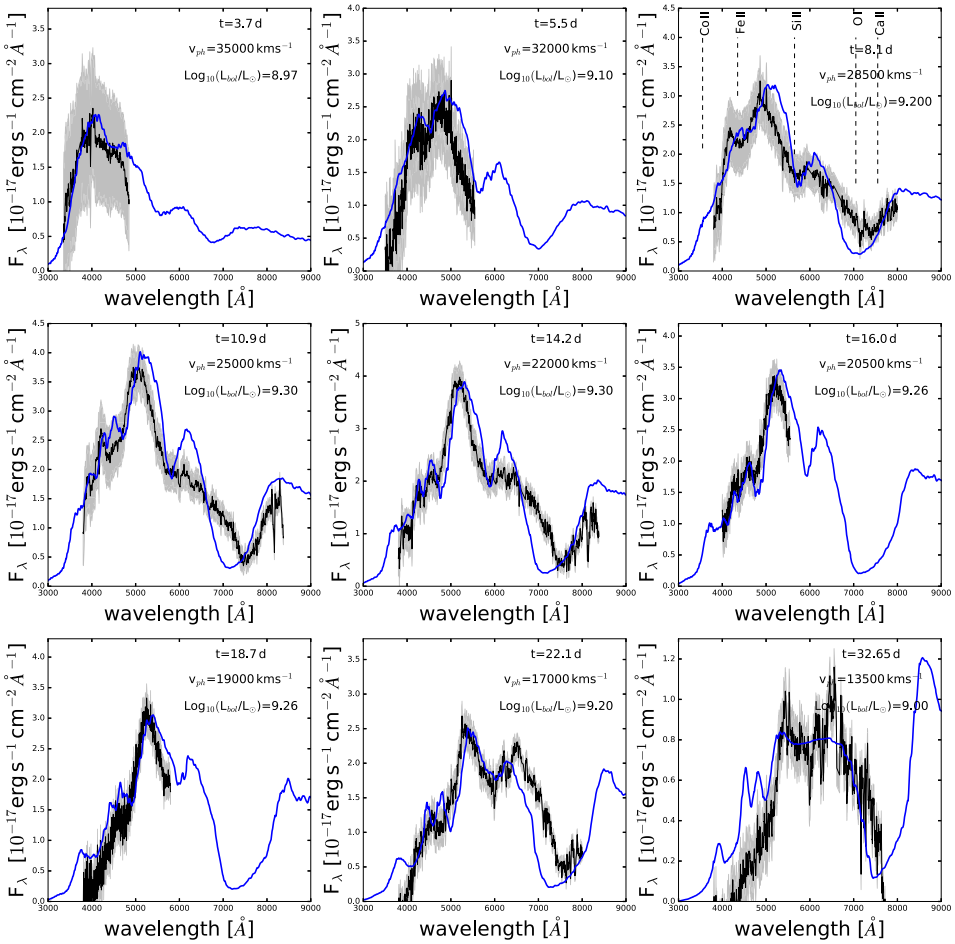

Figure 11. VLT (+FORS2) spectra of SN 2016jca in the rest frame (black) and the best-fitting models (blue) at nine epochs. These models have a decreasing ^{56}Ni abundance as a function of decreasing velocity. The spectra are corrected for Galactic extinction ($E(B-V)_{\rm Gal} = 0.028$ mag) and smoothed with a 15 Å boxcar. The host galaxy and afterglow components were subtracted. The shaded grey region represents the uncertainty related to afterglow subtraction.

Table 3. Input parameters for the spectral models.

Epoch (rest-frame days)	$v_{\rm ph}$ (km s^{-1})	L log($L/L_\odot$)
3.73	35,000 ± 7000	8.97 ± 0.1
5.52	32,000 ± 6400	9.10 ± 0.05
8.11	28,500 ± 2850	9.20 ± 0.02
10.89	25,000 ± 1250	9.30 ± 0.02
14.20	22,000 ± 1100	9.30 ± 0.02
15.96	20,500 ± 1035	9.26 ± 0.02
18.71	19,000 ± 950	9.26 ± 0.02
22.12	17,000 ± 850	9.20 ± 0.02
32.65	13,500 ± 675	9.00 ± 0.02

have been too faint to be observed by the VLT; hence, no signs of it appear in the late-time observation, as discussed above.

5 DISCUSSION

The full opening angle of GRB 161219B (42° ± 3°) is consistent with only 5 out of 68 previously analysed long-duration GRBs, whose full opening-angle distribution peaks at 10° ± 2° (Fong et al. 2014). It is also significantly larger than that of other low-redshift GRBs which were associated with SNe, whose opening angles can be accurately determined, except for GRBs 980425 and 031203, which showed no apparent jet break (see Table 4). However, correcting the isotropic energy of GRB 161219B (1.6×10^{50} erg; Frederiks et al. 2016) for the solid angle subtended by the jet aperture, an intrinsic jet energy of $\sim 10^{49}$ erg is obtained, which is similar to all other events after correcting for collimation. The large opening angle may be the consequence of the widening of the jet after it emerges from the star. In fact, it is unlikely that a jet can carve a 'cone' of ∼42° in the stellar envelope, as this would require a very large amount of energy. Initially jets are probably well collimated, and they can widen only after they break out of the stellar surface (Mizuta & Ioka 2013). So, in the case of GRB 161219B, a larger opening angle would correspond to a smaller amount of energy per solid angle, with the total remaining roughly constant. In GRB-SNe with smaller jet opening angles the widening may have been less significant, or we may have seen the events more on axis if the energy was not uniformly distributed over angle after the jets widened.[1] It should also be noted that the energy observed in

[1]This scenario may also explain why GRB 980425 had such a small isotropic $E_{\rm kin}$ ($\sim 10^{48}$ erg): if the event was observed 10°–15° off axis, as suggested by nebular spectroscopy of SN 1998bw (Maeda et al. 2002), the jet may have spread out significantly. If the energy was not uniformly distributed after jet widening, but more peaked towards the jet axis, the value of

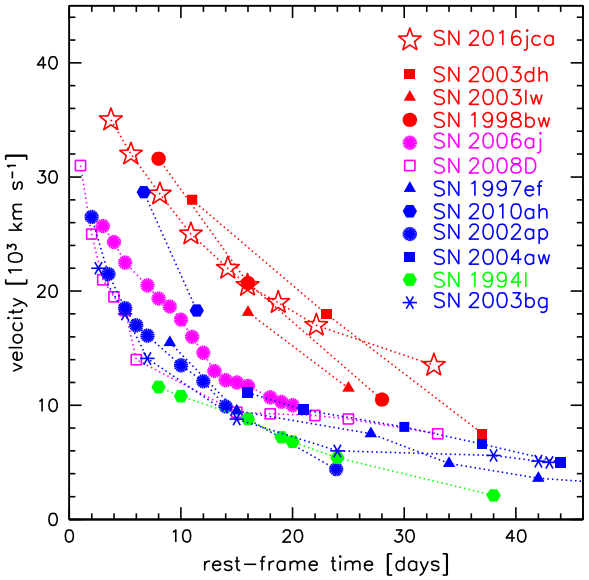

Figure 12. Photospheric velocity, as determined from spectral models, as a function of time from explosion for 12 modelled SNe. The red points are GRB-SNe, the pink points are SNe associated with X-ray flashes. The blue symbols are high-$E_{\rm kin}$ SNe with no detected accompanying high-energy event. SN 1994I is a normal SN Ic. The typical uncertainty of $v_{\rm ph}$ is ∼20 per cent.

the GRB cannot be the energy carried by the material that punches a hole in the star: that energy is used up. Rather, the GRB is made by new material that comes out unimpeded. The energy of the GRB depends on the length of time over which the engine was still active after the jet broke out (Lazzati et al. 2012).

We have plotted the location of SN 2016jca on the correlations of ejected mass, $E_{\rm kin}$, mass of progenitor, and ^{56}Ni mass (see Fig. 13). The location of SN 2016jca is similar to that of other GRB-SNe: it has a $E_{\rm kin}/M_{\rm ej}$ ratio of ∼6, consistent with other GRB-SNe. SN 2016jca has an ejected mass of ∼6.5 $M_\odot$, lower than that of other GRB-SNe but larger than less-energetic events that did not harbour GRBs. Revealing that GRB-SNe have ejecta masses which range from 6 to 11 $M_\odot$. Finally, the mass of the progenitor is consistent with an event creating a black hole rather than a neutron star, similar to all other GRB-SNe.

Cano et al. (2017) present an analysis of SN 2016jca; they, too, claim that the luminosity of the SN is powered by radioactive ^{56}Ni decay. Their best-fitting parameters from fitting the SN light curve were that SN 2016jca had $M_{\rm ej} = 5.8\,M_\odot$, $E_{\rm kin} = 5 \times 10^{52}$ erg, and synthesized 0.22 $M_\odot$ of ^{56}Ni. These values are similar to those obtained from our work, and any discrepancies are likely to be due to the simplistic assumptions they use. As explained extensively by Mazzali et al. (2017), the method implemented by Cano et al. (2017) depends on too many simplifying assumptions and therefore cannot yield reliable results. Incidentally, we note that Cano et al. (2017) are confused about the role of a magnetar in our interpretation of SN 2016jca: they make it appear as if we suggest that the magnetar is the source of luminosity. Magnetar energy may be released to produce explosion kinetic energy, and the accompanying nucleosynthesis may lead to the synthesis of ^{56}Ni. However, in our model, radioactivity is the only source of the luminosity. The light curve of SN 2016jca and all other GRB-SNe can be explained simply by radioactive decay input, and this is consistent with nebular-phase observations that can be analysed to yield the Fe mass (currently available only for SN 1998bw and SN 2006aj; Mazzali et al. 2001; Maeda et al. 2007; Mazzali et al. 2007).

Most well-studied GRB-SNe have a remarkably narrow distribution of properties such as luminosity (∼− 18.7 ± 0.2 mag), ejecta mass (∼10 ± 2 $M_\odot$), and $E_{\rm kin}$ (∼4 ± 1 × 10^{52} erg s^{-1} before correction for asphericity); see Mazzali et al. (2017). However, SN 2016jca has a low ejecta mass for a GRB-SN, demonstrating that there is diversity among GRB-SNe. In fact, SN 2016jca may have had a progenitor which came from a zero-age main sequence (ZAMS) star of ∼25–35 $M_\odot$. Regardless, a normal neutrino-driven SN is unlikely to reach high $E_{\rm kin}$ and to produce several 0.1 $M_\odot$ of ^{56}Ni. Based on the similarity of the SN $E_{\rm kin}$ [(1–2) × 10^{52} erg after correcting for asphericity] to the rotational energy of a millisecond pulsar, it has been suggested that magnetars (highly magnetized and rapidly spinning neutron stars) could be viable central engines (Mazzali et al. 2006; Metzger et al. 2011; Mazzali et al. 2014). If rotational energy is released very rapidly, magnetars could provide $E_{\rm kin}$ to the SN ejecta and contribute to nucleosynthesis, leading to the overproduction of ^{56}Ni. Magnetars may also produce GRB jets (Uzdensky & MacFadyen 2007), but it is unclear whether the material in the jet can reach the observed high Lorentz factors.[2]

On the other hand, if the remnant is a black hole, stellar material may accrete onto the black hole, which launches a pair of jets along the rotational axis. In this 'collapsar' scenario the jets may break out of the star and produce GRBs. It is unclear whether the jets can also deposit the energy required to explode the star violently: only (2–3) × 10^{51} erg of energy are required for the jet to penetrate the stellar envelope, and thereafter no coupling occurs (Lazzati et al. 2013). The large SN $E_{\rm kin}$ may be produced in a broader outflow driven by a disc wind, where ^{56}Ni may also be synthesized. Some ^{56}Ni may also be created if the collapse to a black hole is preceded by a short-lived proto-neutron-star phase, outside which energy is deposited.

One possibility is that the star first collapses to a magnetar creating a neutrino-driven explosion aided by magnetar rotational energy in achieving large $E_{\rm kin}$ and ^{56}Ni mass to power the SN ejecta and light curve. To have any significant energy input at early times, the spin period (P) must be less than a few ms and the magnetic field (B) must be ∼1e15 G. The neutron star may quickly collapse to a black hole if it spins down rapidly, and accretion onto the black hole may create the GRB jets and the high-velocity ^{56}Ni.

Regardless of the nature of the central engine, the fact that SN 2016jca had significantly suppressed flux at shorter wavelengths compared to other GRB-SNe indicates that it had a significant amount of ^{56}Ni at high velocity, which may imply that the explosion was aspherical and that our viewing angle must have been close to the jet axis. All of this high-velocity ^{56}Ni (∼0.03 $M_\odot$ of ^{56}Ni above 10 000 km s^{-1}) could not have been made directly in the jet. Alternatively, high-velocity ^{56}Ni could have been produced in the region surrounding the jet as it pushed through the star, dredged up from the centre of the explosion in an broad outflow next to the jet,

$E_{\rm kin}$(iso) obtained from the energy observed several degrees off axis could significantly underestimate the real $E_{\rm kin}$.

[2]Models have been proposed where the magnetar powers the light curve of superluminous SNe via interaction. This is NOT the scenario we envision here. If we used the magnetar energy to power the light curve, a long spindown time would need to be used, and there would not be enough energy at the earliest times to power the SN $E_{\rm kin}$, leaving unanswered the question of how the SN acquires its $E_{\rm kin}$.

Table 4. Properties of GRB-SNe closer than $z = 0.3$. Properties are taken from Mazzali et al. (2014) and references therein.

GRB-SN	z	T90 (s)	$E_{\rm iso}$ (10^{50} erg)	$\theta_{\rm op}$ (deg)	E_{γ} (10^{50} erg)	SN $E_{\rm kin}$ (10^{50} erg)	$M(^{56}{\rm Ni})$ ($M_{\odot}$)	$E_{\rm radio}$ (10^{50} erg)
1	2	3	4	5	6	7	8	9
980425 / 1998bw	0.0085	30	0.010 ± 0.002	180	0.010 ± 0.002	500 ± 50	0.43 ± 0.05	$\sim$0.2
030329 / 2003dh	0.1685	23	150 ± 30	6 ± 2	0.23 ± 0.05	400 ± 100	0.4 ± 0.1	2.5 ± 0.8
031203 / 2003lw	0.1055	40	1.0 ± 0.4	180	1.0 ± 0.4	600 ± 100	0.6 ± 0.1	0.17 ± 0.06
060218 / 2006aj	0.0335	2000	0.53 ± 0.03	180	0.53 ± 0.03	20 ± 6	0.20 ± 0.05	0.020 ± 0.006
100316D / 2010bh	0.059	$>$1300	0.7 ± 0.2	180	0.7 ± 0.2	100 ± 60	0.12 ± 0.02	$\sim$0.2
120422A / 2012bz	0.283	5	2.4 ± 0.8	23 ± 7	0.05 ± 0.02	400 ± 100	0.3 ± 0.1	...
130427A / 2013cq	0.3399	160	8100 ± 800	3 ± 1	4 ± 1	640 ± 70	0.4 ± 0.1	6 ± 2
130702A / 2013dx	0.145	59	6.5 ± 1.0^{a}	14 ± 4	0.05 ± 0.02	300 ± 60	0.3 ± 0.1	20 ± 5
161219B/ 2016jca	0.145	7	1.6	42 ± 3	0.1	400 ± 80	0.30 ± 0.05	...

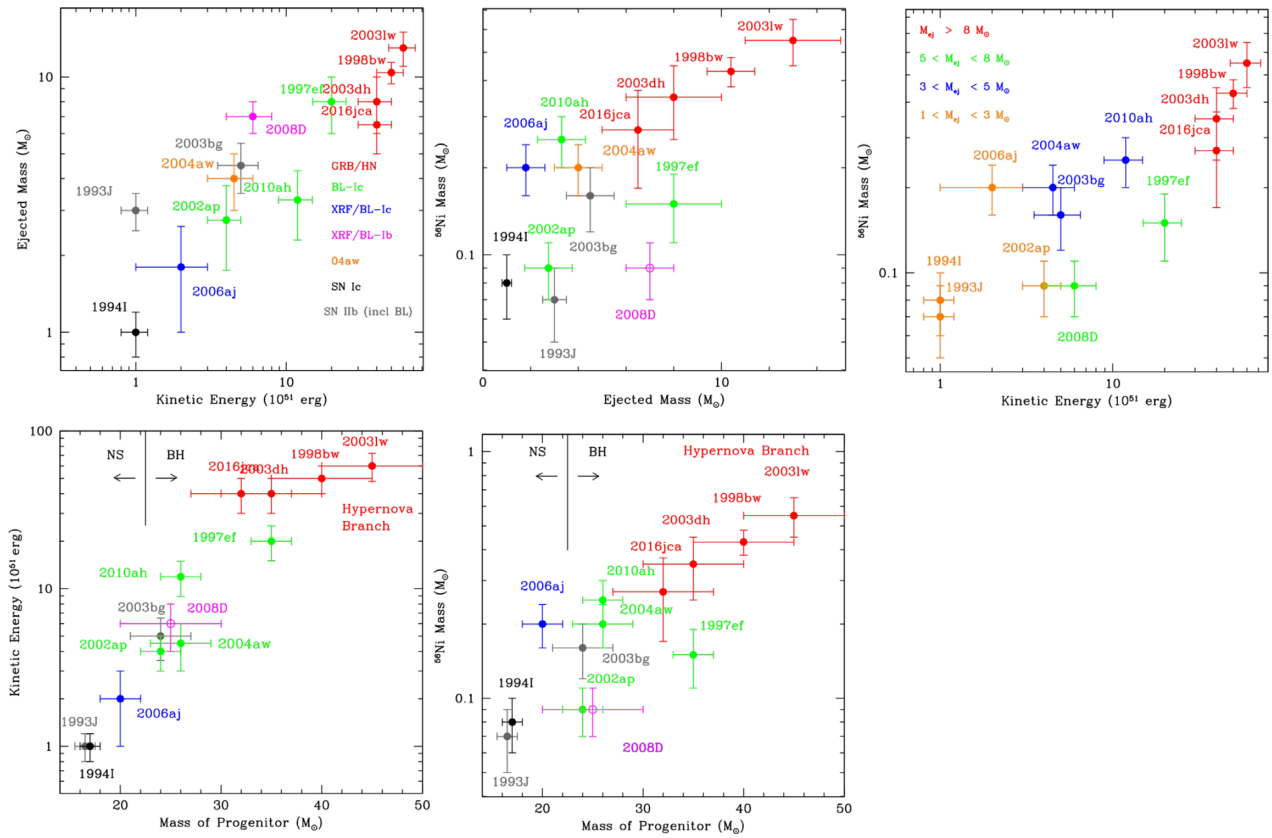

Figure 13. The location of SN 2016jca in terms of the stripped-envelope-SN correlations from Mazzali et al. (2017). For the left and middle panels, the red points are GRB-SNe, the blue points are SNe Ic associated with X-ray flashes, the pink points are SNe Ib associated with X-ray flashes, the black points are normal SNe Ic, and the grey points are normal SNe IIb. For the right top panel the SNe are coloured based on ejecta mass.

or produced in a disc wind around an accreting black hole in the collapsar model.

Recent work has also claimed evidence for high-velocity ^{56}Ni in GRB-SN 2017iuk and an early cocoon generated by the GRB jet (Izzo et al. 2019). However, we note that spectral models of the radial dependence of ^{56}Ni in a GRB-SN, comparison to observations, and a very similar modelling code were first presented and suggested in the original preprint of the present paper.[3] This preprint was first available in 2017 February, two years before the work of Izzo et al. (2019).

[3]https://arxiv.org/abs/1901.05500

6 CONCLUSION

We have presented a multiwavelength analysis of the afterglow of GRB 161219B and the associated SN 2016jca.

A refreshed shock with a luminosity $L(t) \propto t^{-0.85}$, that slows down the time decay of the afterglow, is virtually required by the observed time-decay indices of the X-ray light curve, and it helps solve the mild inconsistency in the fireball closure relationship noted by Cano et al. (2017). Our estimate of the steepening time of the X-ray light curve yields a break time of $\sim$26 d that is formally consistent with that obtained by Cano et al. (2017) ($t_{\rm b} \approx 30$ d), but would cause the SN luminosity to be too low to be compatible with the observed spectra. Therefore, we assumed a break time of $t_{\rm b} = 13 \pm 2$ d, which corresponds to the lower end of the confidence interval we

determined for this parameter. The corresponding full-jet opening angle is $42^\circ \pm 3^\circ$. This turns out to be the widest opening angle that has been calculated for a low-redshift GRB-SNe. However, after correcting for collimation the GRB energy was 10^{49} erg, which is comparable to all previous low-redshift events. This suggests that their underlying engine must be somewhat invariant.

The bolometric light curve of SN 2016jca peaked 12 ± 2 d after explosion at -18.2 ± 0.1 mag. The SN synthesized roughly $0.27 \pm 0.05\,M_\odot$ of ^{56}Ni, but had a more quickly evolving light curve with respect to other GRB-SNe. After correction for afterglow contamination, the spectra of SN 2016jca show suppressed flux at shorter wavelengths with respect to other GRB-SNe. This indicates that there is increased line blanketing in the ejecta of SN 2016jca with respect to other events.

To examine the physics of the SN further we turn to radiative-transfer models. Our models determined that the SN had an ejecta mass of $6.5 \pm 1.5\,M_\odot$ and $E_{\rm kin} = 4 \pm 0.8 \times 10^{52}$ erg, or (1–3) $\times\ 10^{52}$ erg when corrected for asphericity. The models demonstrated that at 3.73 d the photospheric velocity of SN 2016jca was $35\,000 \pm 7200$ km s^{-1}, making this the largest photospheric velocity of any stripped envelope SN. Furthermore, in our models we need a large (0.4 per cent or $0.03\,M_\odot$) ^{56}Ni abundance at high velocities to provide opacity and line blanketing in the blue. In fact, the models favour a decreasing ^{56}Ni abundances as a function of decreasing velocity. This suggests that SN 2016jca was a highly aspherical explosion viewed close to on-axis.

The similarities between the physical properties of GRB-SNe, such as the energy of the GRB when corrected for collimation ($\sim 10^{49-50}$ erg), the $E_{\rm kin}$ of the SN when corrected for asphericity [(1–2)$\times\ 10^{52}$ erg], the average rise time ($\sim$13 d), and the ^{56}Ni mass ($\sim 0.27 \pm 0.05$), demonstrate that these events must have very similar progenitor systems. They could possibly be Wolf-Rayet stars with ZAMS masses of 25–50 $M_\odot$. Furthermore, their central engines must be similar, and there are arguments for and against both the collapsar and magnetar scenarios. Regardless of the nature of central engine, our early-time spectra allowed us to place tight constraints on the $E_{\rm kin}$ of SN 2016jca. The extremely small ratio (<0.1 per cent) between the energy promptly emitted by GRB 161219B in gamma-rays and the kinetic energy of SN 2016jca highlights the fact that the bulk of the energy is carried by the SN and not the jet.

ACKNOWLEDGEMENTS

CA acknowledges support provided by the National Science Foundation (NSF) under grant AST–1613472. Work in this paper was based on observations made with ESO telescopes at the Paranal Observatory under programmes ID 098.D-0055(A), 098.D-0218(A), 298.D-5022(A), and 0100.D-0504(A). MS and SH are supported by a generous grant (13261) from VILLUM FONDEN. MS is also supported by a project grant from the IRFD (Independent Research Fund Denmark). A portion of this work was supported by a grant fron IDA (Danish Instrument Center for Danish Astrophysics). The work of AVF and WZ has been supported by the Christopher R. Redlich Fund, the TABASGO Foundation, and the Miller Institute for Basic Research in Science (U.C. Berkeley). SRO acknowledges the support of the Leverhulme Trust. EP acknowledges Scuola Normale Superiore and INAF for support. AFV thanks the Russian Science Foundation for grant 14-50-00043. AM acknowledges support from the ASI INAF grant I/004/11/1. AJCT acknowledges support from the Spanish Ministry Project AYA2015-71718-R. SW at UCSC was supported by the NASA Theory Program (NNX14AH34G)

Both the Liverpool Telescope and the GTC are operated on the island of La Palma by Liverpool John Moores University in the Spanish Observatorio del Roque de los Muchachos of the Instituto de Astrofisica de Canarias with financial support from the UK Science and Technology Facilities Council. Based on observations made with the TNG, operated on the island of La Palma by the Fundación Galileo Galilei of the Instituto Nazionale di Astrofisica (INAF) at the Spanish Observatorio del Roque de los Muchachos of the Instituto de Astrofisica de Canarias under programme *A32TAC*$_5$. Some of the data presented herein were obtained at the W. M. Keck Observatory, which is operated as a scientific partnership among the California Institute of Technology, the University of California, and the National Aeronautics and Space Administration (NASA); the observatory was made possible by the generous financial support of the W. M. Keck Foundation. We thank the Paranal Director for allocating Discretionary Time to this programme, the Paranal Science Operations team for their assistance, and T. Krühler for assistance with X-Shooter data reduction. This work made use of data supplied by the UK Swift Science Data Centre at the University of Leicester. IRAF is the Image Reduction and Analysis Facility made available to the astronomical community by the National Optical Astronomy Observatories, which are operated by AURA, Inc., under contract with the US National Science Foundation. It is available at http://iraf.noao.edu.

The Pan-STARRS1 Surveys (PS1) and the PS1 public science archive have been made possible through contributions by the Institute for Astronomy, the University of Hawaii, the Pan-STARRS Project Office, the Max-Planck Society and its participating institutes, the Max Planck Institute for Astronomy, Heidelberg, and the Max Planck Institute for Extraterrestrial Physics, Garching, The Johns Hopkins University, Durham University, the University of Edinburgh, the Queen's University Belfast, the Harvard-Smithsonian Center for Astrophysics, the Las Cumbres Observatory Global Telescope Network Incorporated, the National Central University of Taiwan, the Space Telescope Science Institute, NASA grant NNX08AR22G issued through the Planetary Science Division of the NASA Science Mission Directorate, NSF grant AST-1238877, the University of Maryland, Eotvos Lorand University (ELTE), the Los Alamos National Laboratory, and the Gordon and Betty Moore Foundation.

REFERENCES

Ashall C., Mazzali P., Bersier D., Hachinger S., Phillips M., Percival S., James P., Maguire K., 2014, MNRAS, 445, 4427
Ashall C., Mazzali P. A., 2019, preprint (arXiv:submitted)
Ashall C., Mazzali P. A., Pian E., James P. A., 2016, MNRAS, 463, 1891
Ashall C. et al., 2018, MNRAS, 477, 153
Avni Y., 1976, ApJ, 210, 642
Barnes J., Duffell P. C., Liu Y., Modjaz M., Bianco F. B., Kasen D., MacFadyen A. I., 2018, ApJ, 860, 38
Breeveld A. A., Landsman W., Holland S. T., Roming P., Kuin N. P. M., Page M. J., 2011, in McEnery J. E., Racusin J. L., Gehrels N., eds, AIP Conf. Ser. Vol. 1358, An Updated Ultraviolet Calibration for the Swift/UVOT. Am. Inst. Phys., New York, p. 373.
Bufano F. et al., 2012, ApJ, 753, 67
Cano Z. et al., 2017, A&A, 605, A107
Cappellaro E., Mazzali P. A., Benetti S., Danziger I. J., Turatto M., della Valle M., Patat F., 1997, A&A, 328, 203
Cardelli J. A., Clayton G. C., Mathis J. S., 1989, ApJ, 345, 245
D'Elia V. et al., 2015, A&A, 577, A116
Dai Z. G., Cheng K. S., 2001, ApJ, 558, L109

Deng J., Tominaga N., Mazzali P. A., Maeda K., Nomoto K., 2005, ApJ, 624, 898
Dexter J., Kasen D., 2013, ApJ, 772, 30
Drout M. R. et al., 2011, ApJ, 741, 97
D'Ai A. et al., 2016, GCN Circ., 20296
D'Odorico S. et al., 2006, in Society of Photo-Optical Instrumentation Engineers (SPIE) Conference Series, SPIE, Bellingham, p. 626933
Ferrero P. et al., 2006, A&A, 457, 857
Filippenko A. V., 1982, PASP, 94, 715
Filippenko A. V., 1997, ARA&A, 35, 309
Fong W. et al., 2014, ApJ, 780, 118
Frederiks D. et al., 2016, GCN Circ., 20323
Fukugita M., Shimasaku K., Ichikawa T., 1995, PASP, 107, 945
Galama T. J. et al., 1998, Nature, 395, 670
Hjorth J. et al., 2003, Nature, 423, 847
Horne K., 1986, PASP, 98, 609
Israel G. L. et al., 1999, A&A, 348, L5
Iwamoto K. et al., 1998, Nature, 395, 672
Izzo L. et al., 2019, Nature, 565, 324
Janka H.-T., 2012, Annu. Rev. Nucl. Part. Sci., 62, 407
Kasen D., Bildsten L., 2010, ApJ, 717, 245
Kinney A. L., Calzetti D., Bohlin R. C., McQuade K., Storchi-Bergmann T., Schmitt H. R., 1996, ApJ, 467, 38
Lazzati D., Morsony B. J., Blackwell C. H., Begelman M. C., 2012, ApJ, 750, 68
Lazzati D., Villeneuve M., López-Cámara D., Morsony B. J., Perna R., 2013, MNRAS, 436, 1867
Lucy L. B., 1999, A&A, 345, 211
Lyman J. D., Bersier D., James P. A., Mazzali P. A., Eldridge J. J., Fraser M., Pian E., 2016, MNRAS, 457, 328
MacFadyen A. I., Woosley S. E., 1999, ApJ, 524, 262
Maeda K., Nakamura T., Nomoto K., Mazzali P. A., Patat F., Hachisu I., 2002, ApJ, 565, 405
Maeda K. et al., 2007, ApJ, 658, L5
Malesani D. et al., 2004, ApJ, 609, L5
Matheson T. et al., 2003, ApJ, 599, 394
Mazzali P. A., Iwamoto K., Nomoto K., 2000, ApJ, 545, 407
Mazzali P. A., Lucy L. B., 1993, A&A, 279, 447
Mazzali P. A., McFadyen A. I., Woosley S. E., Pian E., Tanaka M., 2014, MNRAS, 443, 67
Mazzali P. A., Nomoto K., Patat F., Maeda K., 2001, ApJ, 559, 1047
Mazzali P. A., Sauer D. N., Pian E., Deng J., Prentice S., Ben Ami S., Taubenberger S., Nomoto K., 2017, MNRAS, 469, 2498
Mazzali P. A., Walker E. S., Pian E., Tanaka M., Corsi A., Hattori T., Gal-Yam A., 2013, MNRAS, 432, 2463
Mazzali P. A. et al., 2002, ApJ, 572, L61
Mazzali P. A. et al., 2006, Nature, 442, 1018
Mazzali P. A. et al., 2007, ApJ, 661, 892
Mazzali P. A. et al., 2008, Science, 321, 1185
Metzger B. D., Giannios D., Thompson T. A., Bucciantini N., Quataert E., 2011, MNRAS, 413, 2031
Mingo B. et al., 2016, GCN, 20298, 1
Mizuta A., Ioka K., 2013, ApJ, 777, 162
Modigliani A. et al., 2010, in Silva D. R. Peck A. B., Soifer B. T., eds, Proc. SPIE Conf. Ser. Vol. 7737, Observatory Operations: Strategies, Processes, and Systems III. SPIE, Bellingham, p. 773728
Oates S. R. et al., 2009, MNRAS, 395, 490
Oke J. B. et al., 1995, PASP, 107, 375
Pian E., Palazzi E., Perley D., 2016, Transient Name Server Discovery Report, 1090
Pian E. et al., 2006, Nature, 442, 1011
Piran T., Nakar E., Mazzali P., Pian E., 2017, preprint (arXiv:1704.08298)
Poole T. S. et al., 2008, MNRAS, 383, 627
Prentice S. J., Mazzali P. A., 2017, MNRAS, 469, 2672
Prentice S. J. et al., 2016, MNRAS, 458, 2973
Prentice S. J. et al., 2018, MNRAS, 478, 4162
Prentice S. J. et al., 2019, MNRAS, 485, 1559
Rhoads J. E., 1999, ApJ, 525, 737
Richmond M. W. et al., 1996, AJ, 111, 327
Sari R., Piran T., Halpern J. P., 1999, ApJ, 519, L17
Sari R., Piran T., Narayan R., 1998, ApJ, 497, L17
Schlafly E. F., Finkbeiner D. P., 2011, ApJ, 737, 103
Stanek K. Z. et al., 2003, ApJ, 591, L17
Steele I. A. et al., 2004, in Oschmann J. M., Jr, ed., Proc. SPIEVol. 5489, Ground-based Telescopes. SPIE, Bellingham, p. 679
Tanaka M. et al., 2009, ApJ, 700, 1680
Tanvir N. R., Kruehler T., Wiersema K., Xu D., Malesani D., Milvang-Jensen B., Fynbo J. P. U., 2016, GCN, 20321, 1
Toy V. L. et al., 2016, ApJ, 818, 79
Ugliano M., Janka H.-T., Marek A., Arcones A., 2012, ApJ, 757, 69
Uzdensky D. A., MacFadyen A. I., 2007, ApJ, 669, 546
Woosley S. E., 1993, ApJ, 405, 273
Woosley S. E., 2010, ApJ, 719, L204
Woosley S. E., 2017, ApJ, 836, 244
Woosley S. E., Bloom J. S., 2006, ARA&A, 44, 507
Zhang W., Woosley S. E., Heger A., 2004, ApJ, 608, 365

APPENDIX A: CONSTRAINTS ON THE RE-ENERGIZED BLAST WAVE

The blast wave that re-energizes the afterglow before it started to be observed is assumed to have a form $L(t) \propto t^{-q}$. We determined q following the formalism of Dai & Cheng (2001) for afterglows produced in uniform media by relativistic electron distributions with a flat spectrum ($p < 2$), and by comparing with the observed decay indices at optical and X-ray wavelengths. The condition that must be satisfied is $q < 1$.

We have

$$E_{\rm tot} \approx E_{\rm inj} \propto t^{1-q},$$

$$\Gamma^2 R^3 \propto t^{1-q},$$

but also $\Gamma^2 R^3 \propto R^{1-q}\Gamma^{2(q-1)}$, because $t \propto R/\Gamma^2$;

then

$$\Gamma \propto R^{-(2+q)/(4-2q)} \propto t^{-(2+q)/8}, \text{ so that } R \propto t^{(2-q)/4}.$$

We have $B \propto \Gamma$ and

$$\gamma_m \propto \Gamma^{1/(p-1)} B^{-(p-2)/[2(p-1)]} \propto \Gamma^{(4-p)/[2(p-1)]},$$

$$\gamma_c \propto \Gamma^{-1} B^{-2} t^{-1}.$$

For the case of a blast wave propagating in a homogeneous medium,

$$\nu_m \propto \Gamma \gamma_m^2 B \propto \Gamma^{(p+2)/(p-1)} \propto t^{-(2+q)(p+2)/[8(p-1)]},$$

$$\nu_{\rm c} \propto \Gamma \gamma_c^2 B \propto \Gamma^{-4} t^{-2} = t^{(q-2)/2}, \text{ and}$$

$$F_{\rm max} \propto N_e \Gamma B \propto N_e \Gamma^2 \propto \Gamma^2 R^3 \propto t^{1-q}.$$

We then have, for $\nu_m < \nu < \nu_{\rm c}$,

$$F_\nu \propto F_{\rm max} \nu_m^{(p-1)/2} \propto t^{1-q} t^{-(2+q)(p+2)/16}.$$

This expression for F_ν must be equivalent to $t^{-\alpha_{\rm opt}}$, from which we derive $\alpha_{\rm opt} = (2+q)(p+2)/16 + q - 1$, which in turn gives $q = 0.85$ for $\alpha_{\rm opt} \approx 0.5$ (observed optical decay index) and $p = 1.66$.

For $\nu > \nu_{\rm c}$, we have

$$F_\nu \propto F_{\rm max} \nu_m^{(p-1)/2} \nu_c^{1/2} \propto t^{-\alpha_{\rm opt}} t^{-(2-q)/4} \propto t^{-\alpha_{\rm X}},$$

Table A1. Secondary standard stars in the field of view of FORS images.

#	α, δ (J2000) (deg)	B (mag)	V (mag)	R (mag)	I (mag)
1	91.67230 − 26.80637	20.671(11)	19.329(06)	18.518(06)	17.678(06)
2	91.67459 − 26.8301	18.380(03)	17.826(05)	17.454(04)	17.086(05)
3	91.69784 − 26.81922	21.895(27)	21.320(27)	20.925(25)	20.557(41)
4	91.71324 − 26.83015	21.810(27)	20.723(14)	20.042(12)	19.407(17)
5	91.71604 − 26.77713	22.030(45)	21.416(45)	20.937(49)	20.425(63)
6	91.72399 − 26.82654	19.903(06)	19.334(06)	18.939(07)	18.540(10)
7	91.73697 − 26.77008	21.223(17)	19.918(09)	19.152(07)	18.397(10)
8	91.73742 − 26.78597	22.547(41)	21.027(20)	20.010(11)	18.579(12)
9	91.74192 − 26.79532	19.325(05)	18.516(05)	18.046(04)	17.583(09)
10	91.74498 − 26.78878	18.638(13)	17.766(11)	17.242(07)	16.750(07)
11	91.75173 − 26.80814	22.006(31)	21.576(32)	21.204(30)	20.866(57)
12	91.75232 − 26.82249	21.161(16)	20.674(15)	20.332(16)	19.944(28)

Note: Numbers in parentheses give the photometric 1σ statistical uncertainty of the secondary standards in units of 10 millimag.

which, for $q = 0.85$, gives $\alpha_X \approx 0.8$, as observed.

[1]*Department of Physics, Florida State University, Tallahassee, FL 32306, USA*
[2]*Astrophysics Research Institute, Liverpool John Moores University, IC2, Liverpool Science Park, 146 Brownlow Hill, Liverpool L3 5RF, UK*
[3]*Max-Planck-Institut für Astrophysik, Karl-Schwarzschild-Str. 1, D-85748 Garching, Germany*
[4]*INAF-OAS Bologna, Via P. Gobetti 93/3, I-40129 Bologna, Italy*
[5]*Department of Astronomy and Astrophysics, University of California, Santa Cruz, CA 95064, USA*
[6]*Astrophysics Research Centre, School of Mathematics and Physics, Queen's University Belfast, Belfast BT7 1NN, UK*
[7]*Department of Physics and Astronomy, Aarhus University, DK-8000 Aarhus C, Denmark*
[8]*Department of Physics, University of Warwick, Coventry CV4 7AL, UK*
[9]*INAF, Astronomical Observatory of Catania, Via Santa Sofia 78, I-95123 Catania, Italy*
[10]*Department of Astronomy, University of California, Berkeley, CA 94720-3411, USA*
[11]*Miller Senior Fellow, Miller Institute for Basic Research in Science, University of California, Berkeley, CA 94720, USA*
[12]*INAF, Brera Astronomical Observatory, Via Santa Sofia 78, I-95123 Catania, Italy*
[13]*Dark Cosmology Centre, Niels Bohr Institute, University of Copenhagen, Juliane Maries Vej 30, DK-2100 København ø, Denmark*
[14]*Instituto de Astrofisica de Andalucia (IAA-CSIC), Glorieta de la Astronomia, E-18008 Granada, Spain*
[15]*Department of Astronomy and Space Sciences, Istanbul University Beyazid, Istanbul 34119, Turkey*
[16]*Mullard Space Science Laboratory, University College London, Holmbury St. Mary, Dorking, Surrey RH5 6NT, UK*
[17]*Space Telescope Science Institute, 3700 San Martin Dr., Baltimore, MD 20218, USA*
[18]*University of California, Berkeley, Space Sciences Laboratory, 7 Gauss Way, Berkeley, CA 94720-7450, USA*
[19]*European Southern Observatory, Karl-Schwarzschild-Str. 2, D-85748 Garching bei München, Germany*
[20]*Kavli Institute for the Physics and Mathematics of the Universe (WPI), The University of Tokyo, Kashiwa, Chiba 277-8583, Japan*
[21]*National Astronomical Observatory of Japan, Mitaka, Tokyo 181-8588, Japan*
[22]*Special Astrophysical Observatory, Nizhnij Arkhyz, Karachai-Cherkessian Republic 369167, Russia*

This paper has been typeset from a TEX/LATEX file prepared by the author.